

Robust H_∞ control of miniaturized optical image stabilizers against product variabilities

Alireza Alizadegan, Pan Zhao, Ryoze Nagamune ^{*}, Mu Chiao

Department of Mechanical Engineering, The University of British Columbia, Vancouver, BC, Canada V6T1Z4

ARTICLE INFO

Keywords:

Optical image stabilizer
Lens-tilting
Mobile phone camera
Product variabilities
Robust control

ABSTRACT

This paper presents uncertainty modeling and robust controller design for 3 degrees-of-freedom miniaturized optical image stabilizers (OISs) against product variabilities. To develop a mathematical model of OISs with product variations, both model and uncertainty structures are determined by finite element analysis. The model parameters are identified based on experimental frequency responses. A robust H_∞ controller design method is applied to the model, in order to guarantee robust stability of the closed-loop system and optimize OIS performance against the hand-induced vibrations of the OIS body. The proposed modeling and controller design method is experimentally validated with large-scale OIS prototypes. The experimental results demonstrate that the robust H_∞ controller outperforms conventional and μ -synthesis controllers.

1. Introduction

Cameras in mobile phones are the most popular due to their availability and portability; however, image blur caused by involuntary hand-shake is an obstacle to their image quality (Hao, Cheng, Kang, & Jiang, 2015). Image stabilization is referred to techniques for alleviating this blur with either software-based or hardware-based approaches. Hardware-based approach to image stabilization and the corresponding device are respectively called *optical image stabilization* and *optical image stabilizer* (OIS). This approach provides better performance compared to software-based one, but is only set back by cost and size limitations of the hardware that has to be integrated with mobile phone camera modules. Therefore, general research trend in this approach has been to develop low-cost miniature OIS with superior rejection of hand-shake effects. Optical image stabilization compensates for hand-shake by restoring the image to its original position on the image sensor. This can be achieved by adjusting either lens or image sensor.

So far, a lot of the OIS research has been focused on sensor-shifting design because in large-scale cameras lenses are heavy and replaceable, thus rendering lens-based OIS cost- and size-inefficient due to additional mechanical features needed to hold and replace heavy lenses. In sensor-shifting OIS, the image sensor is mounted on a moving frame. The moving frame can shift by ball bearings on a stationary frame, and is actuated by a voice coil motor (VCM). Primarily, open-loop controllers were used for position control of the moving frame (Lee, Kook, & Kong, 2012); however, open-loop controllers cannot deal with friction

disturbances inherent in ball bearings. Therefore, feedback controllers such as proportional–integral–derivative (PID) and lead–lag controllers are preferred (Yeom, Park, & Jung, 2007). Moreover, the VCM has non-linear dynamics which may dictate conservative controller design. To address this conservatism, a modified PID controller with a feedforward component was proposed to quickly respond to disturbances (Lee & Kong, 2014). Another potential issue of sensor-shifting design is time-varying dynamics caused by time-varying effects of ball bearings and gravity on the moving frames. To increase robustness of the closed-loop system against these dynamics variations, numerous techniques such as fuzzy (Chang, Kim, Song, & Choi, 2009), gain-scheduling (Yeom, 2009), and sliding mode (Palm, 1994; Tzafestas & Rigatos, 1999; Yu & Liu, 2008b), adaptive (Yu & Liu, 2008a) and a combination of these techniques (Li & Chen, 2013; Li, Chen, & Su, 2012) have been employed.

To circumvent size and cost limitations of sensor-shifting OIS, conceptual design of a novel magnetically-actuated lens-tilting OIS for mobile phone cameras has recently been published (Pournazari, Nagamune, & Chiao, 2014). This mechanical design has following advantages:

- (A1) suitable for inexpensive microfabrication techniques such as micro-molding (Heckele & Schomburg, 2004) and 3D printed molding (Yuan, 2015).
- (A2) no additional actuators are necessary for auto-focus as this design can simultaneously accomplish image stabilization and auto-focus.

^{*} Corresponding author.

E-mail addresses: a.r.alizadegan@gmail.com (A. Alizadegan), nagamune@mech.ubc.ca (R. Nagamune).

- (A3) the energy loss in the proposed OIS operation is minimal because its low-friction mechanical design
- (A4) features magnetic actuator that is faster, cheaper, and more efficient than thermal (Lin & Chiou, 2011) and piezo (Yan, Liu, & Feng, 2015) while avoids snap of electrostatic actuator (Kwon, 2004)
- (A5) can be actuated by moving-magnet actuators smaller than common voice-coil-motor actuators (Chiu, Chao, Kao, & Young, 2008; Komori & Hirakawa, 2005; Song et al., 2010)

Despite these advantages of the lens-tilting OIS proposed in Pournazari et al. (2014), its feedback control has not been fully investigated. A state-feedback controller was designed in Pournazari et al. (2014) and tested only with a single DOF mimicking prototype, which is significantly different from the conceptual design with 3 DOFs. Besides, the product variability was not considered in controller design, even though it has been demonstrated to be important in control of similar small-scale devices, such as single-stage (Harno & Woon, 2015) or dual-stage (Herrmann & Guo, 2004; Huang, Horowitz, & Li, 2005; Huang, Nagamune, & Horowitz, 2006; Li & Horowitz, 2001; Nagamune, Huang, & Horowitz, 2010) hard disk drives micro-actuators, parallel-plate electrostatic micro-actuators (Li & Liu, 2009; Zhu, Penet, & Saydy, 2006), micro/nano-positioning systems (Lee & Salapaka, 2009), micro-probes (Sun, Fowkes, Gindy, & Leach, 2010; Zhang, Koo, Salapaka, Dong, & Ferreira, 2014), optical switches (Izadbakhsh & Rafiei, 2008), gyroscopes (Fei & Batur, 2007; Fei & Zhou, 2012; Li & Liu, 2011), resonators (Sarraf, Sharma, & Cretu, 2011, 2012), relays (Malisoff, Mazenc, & de Queiroz, 2008), and capacitors (Shavezipur, Ponnambalam, Khajepour, & Hashemi, 2008), in the past decade.

As far as product variabilities of the 3 DOF lens-tilting OIS are concerned, a robust controller design method based on μ -synthesis theory was applied to OIS models with synthetic product variabilities and verified in simulations (Alizadegan, Zhao, Nagamune, & Chiao, 2016). However, the order of μ -synthesis controller was too high for practical implementation on a microcontroller in a mobile phone. Zhao, Alizadegan, Nagamune, and Chiao (2015) used a set of large-scale prototypes to show feasibility of the μ -synthesis controller in an experimental setting and its capability to deal with physical product variabilities. To implement the designed μ -synthesis controller, a model order reduction procedure was employed to enable implementation on a dSPACE rapid control prototype (RPC) and its success in stabilization of the closed-loop system for perturbed OISs was demonstrated compared to a lead-lag compensator designed for the nominal prototype. However, a microcontroller in a mobile phone is computationally not as powerful as the dSPACE RPC with, and may not be able to handle even the reduced-order μ -synthesis controller (Song, Gillella, & Sun, 2015). Another challenge is that the μ -synthesis theory suffers from conservatism due to considering the entire uncertainty region and nonconvex optimization which may limit the closed-loop bandwidth. Finally, in Zhao et al. (2015) μ -synthesis was merely compared to a lead-lag compensator only on one disturbance signal that was generated synthetically through a computer and demonstrated on only one perturbed OIS prototype.

This paper proposes a robust H_∞ controller design method for batch-fabricated miniaturized OISs to mitigate the hand-shake induced image blur. The contribution of the proposed method is that it designs a robust controller with fixed order and less conservatism compared to the μ -synthesis controller. Finite element analysis (FEA) is performed to determine both model and uncertainty structures. Based on these structures, a multi-model representation of the uncertainties is developed that represents product variabilities with minimal conservatism by only accounting for vertices of the uncertainty region in design. A robust H_∞ controller with a fixed order is designed via application of linear matrix inequality (LMI)-based controller design theory (Kanev, Scherer, Verhaegen, & de Schutter, 2004) to guarantee the closed-loop stability and optimize the closed-loop performance against uncertainties. The proposed method also features a systematic method to improve

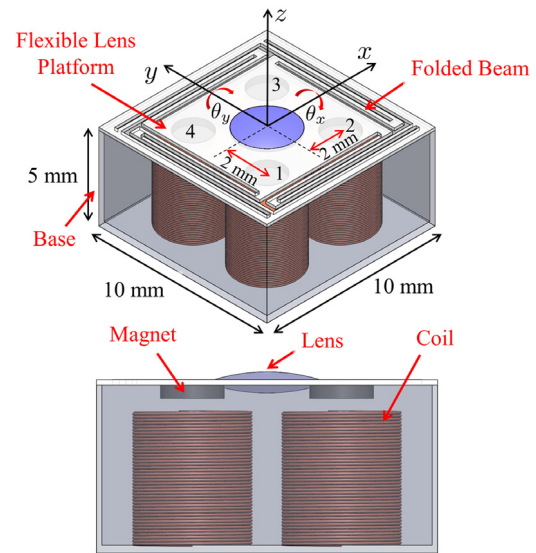


Fig. 1. Mechanical layout for conceptual design of OIS presented in Pournazari et al. (2014).

performance of the initial guess of the controller that leads to enhanced performance of the designed controller. The advantages of the proposed robust H_∞ controller is experimentally validated using real hand-shake signals recorded on a mobile phone, through comparisons with several existing controllers including a μ -synthesis controller presented in Zhao et al. (2015). Moreover, robustness of closed-loop stability and performance for different prototypes are tested and analyzed. It turns out that the robust H_∞ controller outperforms the μ -synthesis controller in performance and controller order.

The paper is organized as follows: Section 2 reviews mechanical design and general control system configuration of the miniaturized OIS system proposed in Pournazari et al. (2014). For the reviewed OIS, in Section 3, model and uncertainty structures are determined based on finite element analysis. Using the structures, details of the proposed robust H_∞ controller design method are presented in Section 4. To validate the model and the robust controller design method, Section 5 gives experimental results on large-scale OIS prototypes, and performance comparisons with conventional controllers.

2. Magnetically-actuated lens-tilting OIS

In this section, we review mechanical design and general control system configuration of the magnetically-actuated lens-tilting OIS introduced in Pournazari et al. (2014) which will be used in this paper.

2.1. Mechanical design

Fig. 1 shows a schematic for mechanical design of the miniature OIS presented in Pournazari et al. (2014). The lens is mounted on a monolithic flat structure referred to as the lens-platform. The lens-platform encompasses a plate supported by four folded beams connecting the plate to the base. The monolithic flat structure makes the design suitable for inexpensive fabrication (A1). The folded beams work as linear springs providing sufficient stiffness for tilting of the plate. The plate has 3 DOFs: two rotational DOFs about x -axis and y -axis for image stabilization as well as a translational DOF along z -axis for auto-focus (A2). The friction in DOFs comes merely from air damping and material damping leading to a low-friction design (A3). Actuation of 3 DOFs is achieved by four moving-magnet actuators (A3 and A4) installed in four corners of the device, marked by 1–4 in Fig. 1 and located in equal distances from central axes. The lens platform shifts along z -axis by

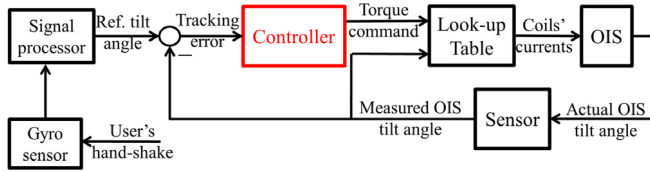


Fig. 2. General control system block-diagram for one rotational DOF of the magnetically-actuated lens-tilting OIS proposed in Pournazari et al. (2014).

Table 1

Parameter values of moving-magnet actuators proposed for conceptual design of the OIS presented in Pournazari et al. (2014).

Component	Parameter	Value	Unit
Coil	Inner diameter	1.0	mm
	Outer diameter	4.1	mm
	Height	4.0	mm
	Wire gauge	36	AWG ^a
	Turns	372	–
Magnet	Diameter	2.5	mm
	Thickness	0.65	mm
	Air-gap at equilibrium	0.25	mm

^a American wire gauge.

application of forces of equal magnitude and direction on all magnets. It tilts about x -axis if forces on magnets 1 and 2 have same magnitude and opposite direction with the ones on magnet 3 and 4. Similarly, tilting about y -axis is actuated by applying forces on magnets 1 and 4 that have same magnitude and opposite direction with the ones on magnet 2 and 3. Each moving-magnet actuator consists of a pair of coil and magnet. Magnets are attached to the lens platform whereas coils are fixed to the base. Actuation is achieved by forces generated on each magnet in response to the magnetic fields created by the current in its corresponding coil. Parameter values of moving-magnet actuators for miniature conceptual design in Pournazari et al. (2014) are shown in Table 1.

This conceptual design has pros and cons. The monolithic flat structure of the lens-platform makes it suitable for low-cost MEMS fabrication methods; however, these methods are afflicted by significant product variabilities. Besides, using moving-magnet actuators to achieve tilt actuation is a quite low-cost solution; however, unavoidable asymmetry in installation of coils as well as misalignments between coils and magnets can lead to couplings in dynamics of different DOFs. Moreover, these couplings are uncertain because asymmetry of installation can appear in different ways for different products. These challenges inherent to this conceptual design will be tackled with the robust control technique in this paper.

2.2. General control system configuration

The miniature OIS in the previous subsection is to be embedded into a mobile phone. As far as image stabilization is concerned, the OIS's main function is to tilt the lens-platform about rotational DOFs to counteract the vibration of the phone body. For OIS function, the general control goal is to use current of individual coils appropriately to tilt the lens-platform to a desired angle according to hand-shake disturbance signals supplied by the mobile phone built-in gyro sensor. A general control system configuration in Fig. 2 was proposed in Pournazari et al. (2014) to achieve this control goal for each rotational DOFs independently.

The hand-shakes disturbances are detected by the gyro sensor of the mobile phone and integrated once to obtain the tilt angle of the camera due to hand-shake. The camera angle is used to calculate, in 'Signal processor' block in Fig. 2, the desired tilt angle of the lens that compensates for the tilt angle of the camera. The error signal

is acquired by subtracting the measured tilt angle from the reference tilt angle. Based on the error, the controller sends appropriate current commands to four coils in order to tilt the lens-platform for minimizing the error. The moving-magnet actuators, which generate torque from applied current, are non-linear systems due to the dependence of the magnetic force from each actuator on the air gap; however, since this non-linearity is static, it can be compensated for via a static map, that is the inverse of the map from the current to the torque. This is designated as 'Look-up Table' in Fig. 2, and explained in detail in Appendix A. Therefore, throughout this paper, controllers are designed by considering the torque as the control input, and the OIS system as a linear system.

2.3. Performance specifications and objectives

The performance considerations proposed in this paper include four specifications and four objectives. Performance specifications refer to hard constraints that have to be met, while performance objectives are performance measures that we wish to improve. Specifications are precedent to objectives and both are listed below in a descending order of priority. Performance specifications include:

- (S1) stability of closed-loop system,
- (S2) minimal steady-state error,
- (S3) upper limit on peak sensitivity gain to allow sufficient stability margin for modeling errors, and
- (S4) upper limit on high-frequency controller gain to avoid actuator saturation due to sensor noise amplification.

On the other hand, the objectives are to:

- (O1) minimize tracking error to improve image blur,
- (O2) minimize control effort to increase battery life,
- (O3) reduce degradation of performance objectives (O1) and (O2) against product variabilities, and
- (O4) reduce controller order for practical implementation and computation power consumption considerations on a mobile phone.

Tracking error is measured by calculating the root mean square (RMS) value of the tracking error signal, and control effort is assessed by calculating the integral of absolute current values over time.

3. Finite element analysis

To propose a physics-based dynamic uncertainty model in the next section, an FEA is performed in this section to identify dynamics of OIS as well as effect of uncertainties in beam width and actuator installation on dynamics of OIS. Fig. 3 shows eigenfrequency analysis results. The first four modes which are associated with four eigenfrequencies denoted by ω_{n_i} , $i = 1, 2, 3, 4$. The first and second modes are respectively corresponding to shifting and tilting DOFs. The DOFs associated with the third and fourth mode are not trivial to explain based on mode shapes. Therefore, they are identified through performing frequency response analyses on dynamics of shifting and tilting DOFs in the next step.

To identify the dynamics of shifting and tilting DOFs, the frequency response of the lens-platform to translational and rotational actuation is obtained. Only one of the tilting DOFs are analyzed and modeled because tilting DOFs about x - and y -axis are similar and independent (decoupled). In Figs. 4(a) and 4(b), blue solid lines indicate frequency responses of shifting and tilting dynamics of OIS, respectively. Shifting dynamics only includes shifting mode, while the tilting dynamics has the tilting mode (corresponding to the first peak in Fig. 4(b)) as well as the 3rd and 4th modes (corresponding to the notch and peak between 500 and 1000 Hz in Fig. 4(b)). All of the modes are lightly-damped because of the low-friction mechanical design OIS.

Since the focus in this paper is the tilting, and not the shifting, effects of beam width variation and force imbalance are studied on tilting

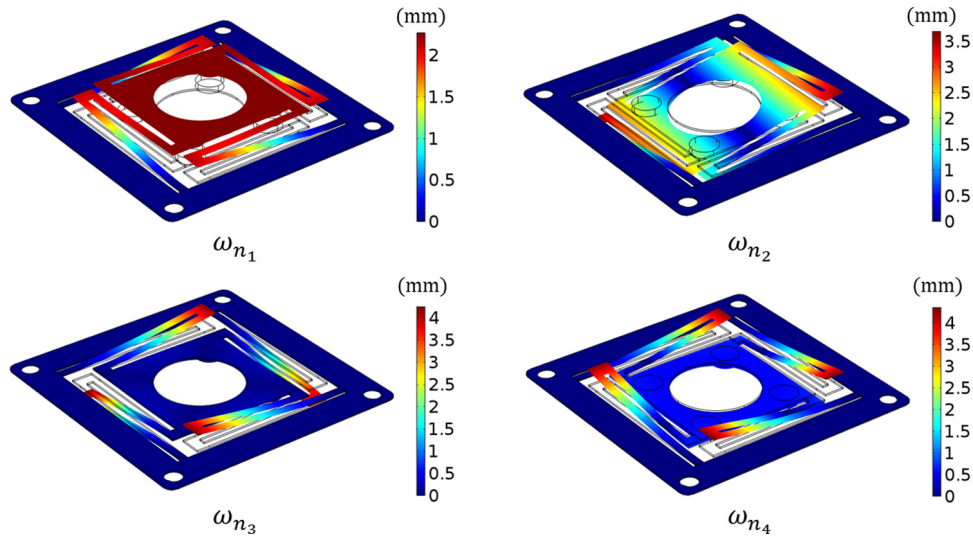
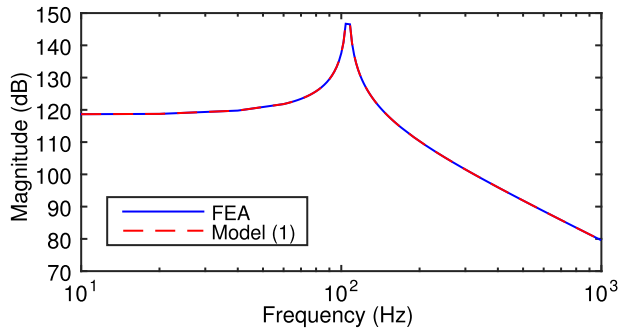
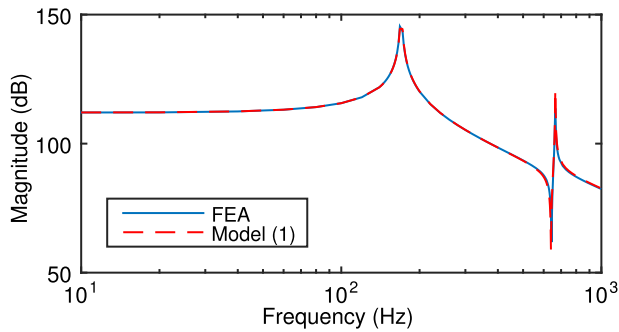


Fig. 3. Eigenfrequency analysis results based on FEA model of the miniaturized OIS.



(a) Shifting dynamics



(b) Tilting dynamics

Fig. 4. Nominal dynamics of FEA model for the miniaturized OIS. (For interpretation of the references to color in this figure legend, the reader is referred to the web version of this article.)

dynamics. Fig. 5(a) illustrates tilting frequency responses of OIS under $\pm 10\%$ variations of the nominal beam width.

Variations in beam width lead to uncertainties in DC gain of tilting dynamics as well as all natural frequencies because the beam width is related to the spring stiffness. To be more specific, the increase of beam width increases stiffness, leading to the decrease in DC gain and the increase in natural frequencies. Fig. 5(b) shows tilting frequency response of OIS under $\pm 10\%$ imbalance in actuator forces. Force imbalance brings about coupling of shifting dynamics with tilting dynamics. As the percentage of force imbalance increases, magnitude of coupling

increases. The damping ratios are roughly the same in either scenarios because they are affected by the material rather than the geometry.

4. Robust controller design method

This section presents a robust controller design method developed for OIS based on FEA. The proposed method encompasses a dynamic uncertainty modeling method and a robust H_∞ controller design method.

4.1. Dynamic uncertainty modeling

The objective of dynamic uncertainty modeling is to develop a mathematical representation of the dynamic behavior of the OIS as well as product variabilities based on FEA. The model considers the torque generated on the lens-platform as the control input and the tilt angle of the lens-platform as the measured output. Based on FEA results, a model of the following structure is proposed:

$$G(s, \delta) = [G_{shift}(s, \delta) + G_{tilt}(s, \delta)]e^{-s\tau}, \quad (1)$$

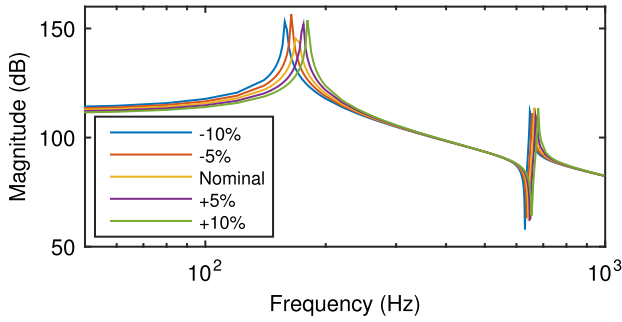
where G_{shift} and G_{tilt} denote the transfer functions corresponding to the coupling of shift dynamics and the tilt dynamics, respectively, and δ designates the uncertainty parameter vector representing product variabilities. For each of these terms, the following model structure is proposed by the inspection of Fig. 4:

$$G_{shift}(s, \delta) = \frac{K_{shift}\omega_{n1}^2}{s^2 + 2\xi_1\omega_{n1}s + \omega_{n1}^2}, \quad (2)$$

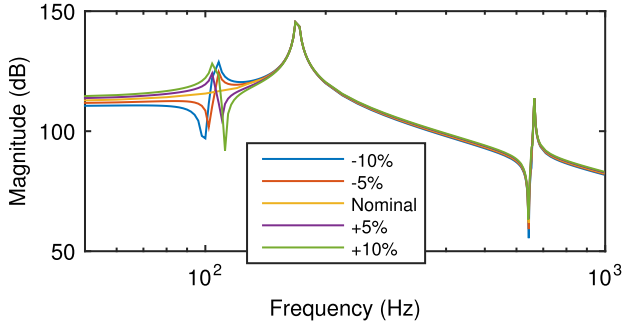
$$G_{tilt}(s, \delta) = \frac{K_{tilt}\omega_{n2}^2}{s^2 + 2\xi_2\omega_{n2}s + \omega_{n2}^2} \cdot \frac{\frac{\omega_{n4}^2}{s^2 + 2\xi_4\omega_{n4}s + \omega_{n4}^2}}{\frac{\omega_{n3}^2}{s^2 + 2\xi_3\omega_{n3}s + \omega_{n3}^2}}, \quad (3)$$

where ω_{ni} and ξ_i are respectively natural frequency and damping ratio of the i th mode. K_{shift} and K_{tilt} are DC-gains of the coupling mode and tilt dynamics, respectively. In (1), τ is the time-delay of the amplifier circuit that will be identified experimentally and approximated by a linear transfer function using Padé approximation.

Product variabilities are represented by parametric uncertainties δ in (1). Based on FEA results, natural frequencies and DC-gains are considered uncertain while the damping ratios are assumed to be fixed. K_{shift} is considered as a standalone uncertainty parameter representing



(a) Beam width variations



(b) Force imbalances

Fig. 5. Effect of product variabilities in conceptual design on tilting dynamics based on FEA.

force imbalance (Fig. 5(b)), while ω_{n_2} is the uncertainty parameter representing beam width variations (Fig. 5(a)). Therefore, two independent uncertainty parameters are defined as

$$\delta := [K_{shift}, \omega_{n_2}]. \quad (4)$$

The independent uncertainty parameters vary between an upper-bound and lower-bound as follows:

$$\underline{K_{shift}} < K_{shift} < \overline{K_{shift}}, \quad (5)$$

$$\underline{\omega_{n_2}} < \omega_{n_2} < \overline{\omega_{n_2}}, \quad (6)$$

where underline and overline represent respectively the lower- and upper-bound of each uncertainty parameter that will be identified experimentally.

Uncertainties in ω_{n_i} , $i = 1, 3, 4$, and k_{ilt} are related to uncertainties in ω_{n_2} because they are due to the same mechanical origin (beam width variations). Furthermore, this correlation leads to a control-oriented model (a small number of uncertainty parameters) that can be dealt with by the robust control theories. The correlations in these parameters are found as follows:

$$k_{ilt} = k_{ilt}^* \left(\frac{\omega_{n_2}^*}{\omega_{n_2}} \right)^{2c_k}, \quad \omega_{n_i} = \omega_{n_i}^* \left(\frac{\omega_{n_2}}{\omega_{n_2}^*} \right)^{c_i}, \quad i = 1, 3, 4, \quad (7)$$

where the superscript * denotes the nominal values of dynamics parameters to be identified experimentally. The correlation parameters c_i , $i = 1, 3, 4$ and c_k are used to account for the increased complexity of the lens-platform structure compared to a simple mass–spring–damper system. According to FEA, we found parameter values as $c_1 = 1.1$, $c_3 = 0.3$, $c_4 = 0.4$, and $c_k = 1.7$.

To validate the model structure (1), nominal frequency responses of model (1) and FEA model are compared in Fig. 4. As shown, the proposed model structure accurately describes the dynamics of

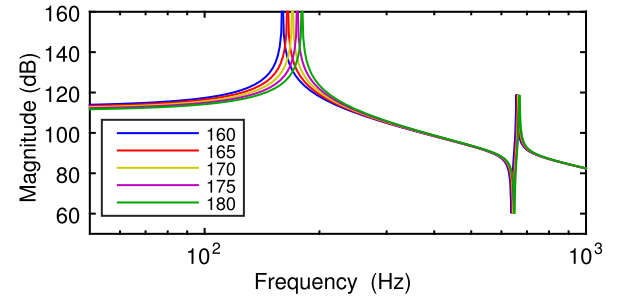
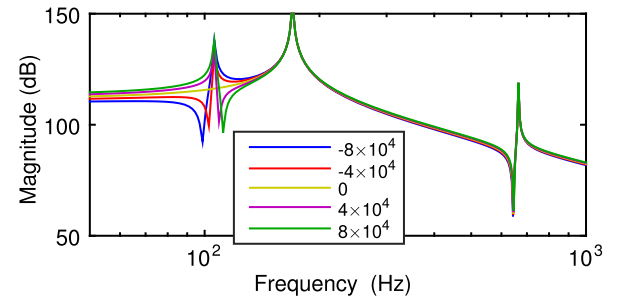
(a) ω_{n_2} uncertainties(b) K_{shift} uncertainties

Fig. 6. Effect of uncertainty parameters K_{shift} and ω_{n_2} on frequency response of model (1).

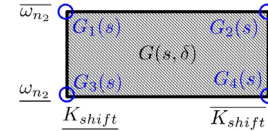


Fig. 7. Illustration of uncertainty region and definition of multi model $G_i(s)$, $i = 1, 2, 3, 4$.

the system. To validate uncertainty modeling, samples of frequency responses obtained by varying K_{shift} and ω_{n_2} in (1) are compared with samples of frequency responses obtained by varying force imbalance and beam width in FEA model, respectively. Fig. 6(a) shows samples of the uncertainty model (1) when ω_{n_2} is increased from 160 Hz to 180 Hz with 5 Hz increment. Similarly, Fig. 6(b) corresponds to variation of K_{shift} from -8×10^4 to 8×10^4 with 4×10^4 increments. By comparing these samples with Fig. 5, it can be seen that K_{shift} and ω_{n_2} provide a decent representation of force imbalance and beam width variation, respectively.

Based on independent uncertainty parameters K_{shift} and ω_{n_2} , the uncertainty region can be represented by a rectangle as illustrated in Fig. 7. With this uncertainty region, two uncertainty models can be defined: real parametric uncertainty model $G(s, \delta)$ and the multi-model $G_i(s)$, $i = 1, 2, 3, 4$. The real parametric uncertainty model considers the area inside the rectangle while the multi-model uncertainty model deals with only the vertices. In this paper, the emphasis is placed on multi-model uncertainty model to design the robust H_∞ controller described in the next subsection. The real parametric uncertainty model is merely used to design the μ -synthesis controller for comparison purposes.

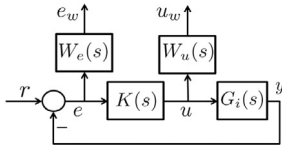


Fig. 8. Weighted control system block-diagram.

4.2. Robust H_∞ controller design

The robust H_∞ control theory is applied to the multi-model uncertainty model. To apply robust H_∞ control theory, a multi-model robust controller is designed based on the weighted control system block-diagram shown in Fig. 8 where e is the tracking error, u is the control input (torque), and y is the measured output (tilt angle). r is the desired tilt angle. e_w and u_w are weighted tracking error and control input signals, respectively. In the figure, the dynamic output-feedback linear time-invariant controller to be designed is denoted by

$$K(s) = \begin{bmatrix} A_K & B_K \\ C_K & D_K \end{bmatrix} \quad (8)$$

where the following notation is used.

$$\begin{bmatrix} A & B \\ C & D \end{bmatrix} := D + C(sI - A)^{-1}B. \quad (9)$$

The block G_i is the multi-model developed in the previous section. The performance channel z is introduced as

$$z := [e_w \quad u_w]^T. \quad (10)$$

The augmented plant corresponding to the block diagram in Fig. 8 is realized in a state-space form of

$$\begin{bmatrix} \dot{z} \\ e \end{bmatrix} = \begin{bmatrix} A_i & B_{r,i} & B_{u,i} \\ C_{z,i} & D_{zr,i} & D_{zu,i} \\ C_{e,i} & D_{er,i} & 0 \end{bmatrix} \begin{bmatrix} r \\ u \end{bmatrix}, \quad (11)$$

where the state-space matrices of the generalized plant can be obtained based on state-space realizations of G_i , W_e , and W_u . The D-matrix relating the signals u and e is zero because the transfer function G_i in Fig. 2 is strictly proper.

The robust H_∞ controller design method guarantees robust stability (S1) and robust performance (O3) by considering uncertainty parameter δ . The weighting function W_e is used to penalize tracking error (O1), reduce steady-state error (S2), and meet stability margin specifications (S3). W_u is a weighting function used to penalize control effort (O2) and avoid saturation due to noise amplification (S4). To avoid undue increase of controller order (O4), we propose using constant W_u and first order W_e parameterized as follows (Zhou, Doyle, & Glover, 1996):

$$W_e(s) = \frac{s/M_H + \omega_b}{s + \omega_b M_L}, \quad (12)$$

where M_L , M_H , and ω_b are design parameters which, respectively, are related to low-frequency gain, high-frequency gain, and 0 dB crossing frequency of W^{-1} . To reduce steady-state error (S2), M_L should be decreased. Tracking error (O1) can be reduced by increasing ω_b . To increase stability margin (S3), peak of sensitivity M_H should be reduced. Finally, W_u is taken as a constant gain, and it is increased to save control effort (O2) and avoid saturation due to noise amplification (S4).

Due to inherent trade-off between performance objectives and specifications, controller design parameters M_L , M_H , ω_b , and W_u are selected such that performance objectives improve while performance specifications are satisfied. To select the controller design parameters, trial-and-error is used rather than optimization because there is no explicit relationship between the controller design parameters and the performance objectives and specifications.

The multi model robust controller design problem is formulated based on a similar formulation in Kanev et al. (2004), as

$$\min_{\Theta} \max_i \|\mathcal{T}_{rz,i}(\Theta)\|_\infty, \quad (13)$$

where $\mathcal{T}_{rz,i}$ is the transfer function from r to z when the plant is set to G_i . According to (10), z includes tracking error (O1) and control effort (O2). In the optimization problem, the matrix variable

$$\Theta = \begin{bmatrix} A_K & B_K \\ C_K & D_K \end{bmatrix} \quad (14)$$

includes state space parameters of the robust controller. The objective function is H_∞ -norm of the closed-loop system, where H_∞ -norm of a stable transfer function $P(s)$ is defined as $\|P\|_\infty := \sup_{\omega} \bar{\sigma}(P(j\omega))$ with $\bar{\sigma}(\cdot)$ denoting the largest singular value. As $\mathcal{T}_{rz,i}(\Theta)$ is the transfer function from r to z (including e and u) weighted in appropriate frequencies by W_e , minimization of this objective function reduces tracking error (O1) and control effort (O2). The maximum over i considers the worst-case performance within multi models G_i , thus giving robustness to the designed controller. The state-space parameters of the closed-loop system $\mathcal{T}_{rz,i}$ can be derived from the state-space parameters of the augmented plant (11) and the controller (14) as follows (see Appendix B):

$$\mathcal{T}_{rz,i}(s) = \begin{bmatrix} A_{0,i} + B_i \Theta C_i & B_{0,i} + B_i \Theta D_{er,i} \\ C_{0,i} + D_{zu,i} \Theta C_i & D_{zr,i} + D_{zu,i} \Theta D_{er,i} \end{bmatrix} \quad (15)$$

where the matrices are defined as

$$A_{0,i} := \begin{bmatrix} A_i & 0 \\ 0 & 0 \end{bmatrix}, B_i := \begin{bmatrix} 0 & B_{u,i} \\ I & 0 \end{bmatrix}, C_i := \begin{bmatrix} 0 & I \\ C_{e,i} & 0 \end{bmatrix} \quad (16)$$

$$B_{0,i} := \begin{bmatrix} B_{r,i} \\ 0 \end{bmatrix}, D_{er,i} := \begin{bmatrix} 0 \\ D_{er,i} \end{bmatrix}, C_{0,i} := [C_{z,i} \quad 0], D_{zu,i} := [0 \quad D_{zu,i}] \quad (17)$$

As shown, $\mathcal{T}_{rz,i}$ depends on uncertainty (i) which guarantees robust closed-loop stability and performance (O3). Furthermore, it linearly depends on a controller (Θ) that has order as high as order of the generalized plant. Therefore, controller order can be reduced as desired by appropriate choice of plant model and weighting functions to allow for practical implementation (O4).

By applying the bounded real lemma to (15) (see Appendix C), this problem can be reformulated as the following optimization problem:

$$\text{minimize } \gamma, \text{ subject to } \Psi_i(P_i, \gamma) + Q_i^T \Theta^T P_i(P_i) + P_i(P_i)^T \Theta \Theta_i < 0, \forall i \quad (18)$$

In the optimization problem, γ represents the worst-case tracking error (O1) and control effort (O2) that is minimized through searching for optimum controller parameter Θ . The constraint function repeated for all i makes sure that closed-loop stability (S1) and performance specs (S2–S4) are met for all models in multi model (G_i) by finding its corresponding closed-loop Lyapunov matrix $P_i > 0$. The other matrices can be written as:

$$\Psi_i(P_i, \gamma) := \begin{bmatrix} \langle P_i A_{0,i} \rangle & P_i B_{0,i} & C_{0,i}^T \\ * & -\gamma I & D_{zr,i}^T \\ * & * & -\gamma I \end{bmatrix}, \quad (19)$$

$$P_i(P_i) := [B_i^T P_i \quad 0 \quad D_{zu,i}^T], Q_i := [C_i \quad D_{yr,i}^T \quad 0]. \quad (20)$$

where for a generic matrix A , the symbol $\langle A \rangle$ is defined as $\langle A \rangle = A + A^T$. In above equations, Ψ_i are affine with respect to P_i and γ , P_i are affine with respect to P_i , and Q_i are constant matrices. Therefore, even though the problem is non-convex due to coupling of P_i and Θ , it is convex with respect to P_i and Θ individually. In other words, assuming P_i is the decision variable and Θ is a fixed parameter or Θ is the decision variable and P_i is a fixed parameter, the problem becomes convex. Using this property, a sequential design procedure is employed to solve the optimization problem (18) as follows:

- 1 Employ the procedure in Appendix D to solve for an initial feasible solution. Set the result of this procedure as Θ_1 and set $k = 1$.
- 2 Set $\Theta := \Theta_k$ and solve the convexified form of problem (18) with respect to γ and P_i . Denote the solution for γ and P_i as γ_k and $P_{i,k}$, respectively.
- 3 Set $P_i := P_{i,k}$ and solve the convexified form of problem (18) with respect to γ and Θ . Denote the solution for γ and Θ as γ_{k+1} and Θ_{k+1} , respectively.
- 4 If $\gamma_k - \gamma_{k+1} > \epsilon$ for a specified tolerance $\epsilon > 0$, set $k := k + 1$ and go to step 2; otherwise, Θ_k is the parameter matrix of the designed controller.

As problem (18) is nonconvex, the optimal solution may not be obtained through this sequential algorithm; nevertheless, since γ is monotonically nonincreasing during the iterations and it has a lower bound of 0, it will converge to some positive number whereas none of conventional controller design methods attempt such systematic improvement of the designed controller. Even though the final solution may not be the optimal solution to the problem, the systematic enhancement of the controller will lead to a better performance than conventional controllers. This point will be verified through experiments.

To recap, the proposed method provides following advantages:

- It guarantees closed-loop stability and optimizes worst-case closed-loop performance considering uncertainties
- It provides systematic method to obtain good initial guess for optimization to reduce conservatism of controller
- It can deal with non-integer values for correlation parameters to mitigate conservatism of model
- It constrains controller order with order of plant model in controller design stage to reduce controller order

The proposed method is formulated for one of the tilting DOFs; however, as the two tilting DOFs are similar and independent; the method can be similarly applied to both to handle all OIS control of the 3 DOF conceptual design.

5. Experimental results

5.1. Experimental setup

Although this paper develops modeling and controller design method for the miniaturized conceptual design of OIS, we do not use miniaturized prototypes integrated with mobile phone cameras for experimental validation in this paper because the miniaturized prototypes are under development. Furthermore, integration of the miniaturized prototypes with existing mobile phone cameras requires sensor development and instrumentations that are beyond the scope of this paper. The objective of the experimental validation in this paper is to demonstrate feasibility of the modeling and controller design method in an experimental setting and its capability to deal with physical product variabilities. This goal is achieved in this paper by the application of the proposed method to stand-alone large-scale prototypes fabricated rapidly and simply by available general-purpose rapid prototyping facilities. Physical product variabilities are realized by fabrication of five different prototypes, one of which is shown in Fig. 9.

The lens-platform of these prototypes are fabricated with different beam widths to mimic fabrication errors in miniature OISs. These prototypes are denoted by OIS 1 to OIS 5 in an increasing order of beam width. The prototypes are also subject to errors in installation of moving-magnet actuators by hand. The lens platform has a dimension of 6×6 cm. It is made of 17–7 stainless steel and fabricated by a water jet cutter. The lens platform and coils are installed on an aluminium base. The aluminium base features screws for adjusting height of coils. Parameter values of moving-magnet actuators of large-scale prototypes are listed in Table 2.

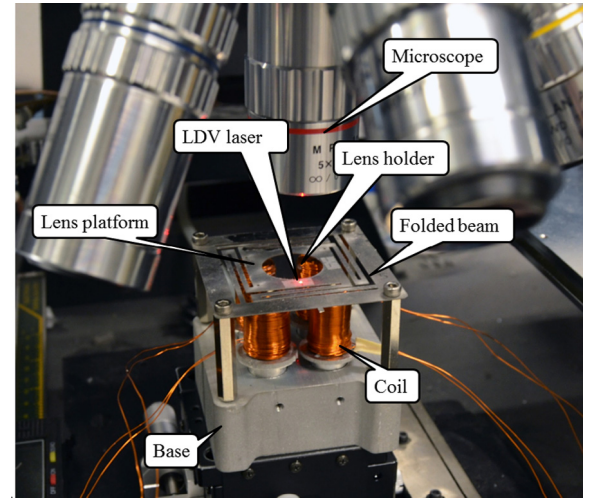


Fig. 9. One example of five different large-scale prototypes fabricated for experimental validation.

Table 2

Parameter values of moving-magnet actuators used in large-scale prototypes fabricated for experimental validation.

Component	Parameter	Value	Unit
Coil	Inner diameter	2.06	mm
	Outer diameter	14.4	mm
	Height	21.5	mm
	Wire gauge	28	AWG
	Turns	960	–
Magnet	Diameter	6.34	mm
	Thickness	1.6	mm
	Air-gap at equilibrium	1	mm

The proposed method is implemented by the experimental setup depicted in Fig. 10. The tilt angle of OIS is measured by a laser Doppler vibrometer (LDV) ('Sensor' block in Fig. 2 for our experimental setup) as voltage signal and fed back to the controller. The actual miniaturized OIS needs to use some other sensors (e.g. hall sensors or strain gauges) that is more suitable for small scale implementation; however, this paper uses LDV for feedback because the experiment is conducted on a large-scale prototype as preliminary study. The LDV has 320 nm resolution and 20 kHz bandwidth which is sufficient to accurately characterize dynamics of the system in high-frequency band. The DS1103 dSPACE controller board is employed for controller implementation by 1 msec sampling rate. It outputs control signal in the form of voltage which is converted to current by an amplifier consisting of a power supply and a circuit. This current is applied to coils to tilt the lens-platform.

5.2. System identification

Nominal values for dynamics parameters in (2) and (3) as well as upper-bounds and lower-bounds of uncertainty parameters in (5) and (6) are identified experimentally based on frequency responses of different prototypes exhibited in Fig. 11. The actuator bandwidth is about 150 Hz. Variations in natural frequencies and DC gain as well as coupling of shifting mode discussed in Section 3 can be observed. As can be seen, with an increase in beam width from OIS 1 to OIS 5, the natural frequencies increase. This trend is similar to the one observed in FEA results in Fig. 5(a). The line colors in Figs. 5(a) and 11 are chosen correspondingly.

The parameters of the proposed uncertainty model are identified based on these frequency response data. Numeric values for nominal natural frequencies and damping ratios of different modes are presented in Table 3. The nominal value for DC-gain of tilting dynamics in (3)

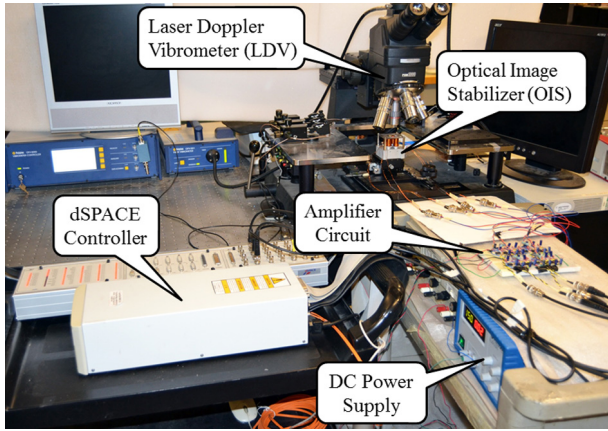


Fig. 10. The experimental setup.

Table 3

Nominal parameter values for uncertainty model (1) representing five large scale prototypes.

	$i = 1$	$i = 2$	$i = 3$	$i = 4$
ω_{n_i} (Hz)	63.84	101.7	229.4	252.4
ξ_{ω_i}	0.005	0.0001	0.001	0.001

Table 4

Bounds of uncertainty parameters for uncertainty model (1) representing five large scale prototypes.

	Lower-bound	Upper-bound
ω_{n_2} (Hz)	96.6	106.8
K_{shift}	−0.2	0.2

is identified as $K_{ilt} = 4.1$, whereas the nominal value for DC-gain of shifting dynamics (K_{shift}) is considered zero assuming no coupling for the nominal system. The time-delay τ is identified as 1.1 msec using the phase shift data. The numeric values for lower-bounds and upper-bounds of uncertainty parameters are identified as listed in Table 4.

The multi-model obtained based on these identified parameters is compared with frequency response data in Fig. 11. It can be seen that variations of natural frequencies for different modes and uncertain coupling of the shifting mode are captured by the model.

5.3. Controller design results

A robust H_∞ controller is designed by the application of the method explained in Section 4.2 to the multi-model. The upper limits for peak sensitivity gain (S3) and controller high-frequency gain (S4) are selected 6 dB and 1 by trial and error for our experimental setup. The parameters selected for designing the robust H_∞ controller are $M_L = -20$ dB, $\omega_b = 5$ Hz, $M_H = 2$ dB, and $W_u = 30$ dB. The proposed method is implemented in MATLAB, where LMIs are solvable efficiently by LMI Toolbox's interior point method-based algorithms. The robust H_∞ controller is designed by 3 iterations in the sequential design procedure leading to performance upper-bound of 1.55.

The designed robust H_∞ controller was compared with four conventional nominal controllers, i.e., PID, lead–lag, linear-quadratic Gaussian (LQG), and H_∞ controller, as well as a conventional robust controller, namely μ -synthesis controller. OIS 3 is used as the nominal plant for design of nominal controllers due to its intermediate dynamical behavior as shown in Fig. 11. To design the μ -synthesis controller, G_i in Fig. 8 is replaced with $G(s, \delta)$. The resulting robust control problem can be solved by MATLAB Robust Control Toolbox (Balas, Chiang, Packard,

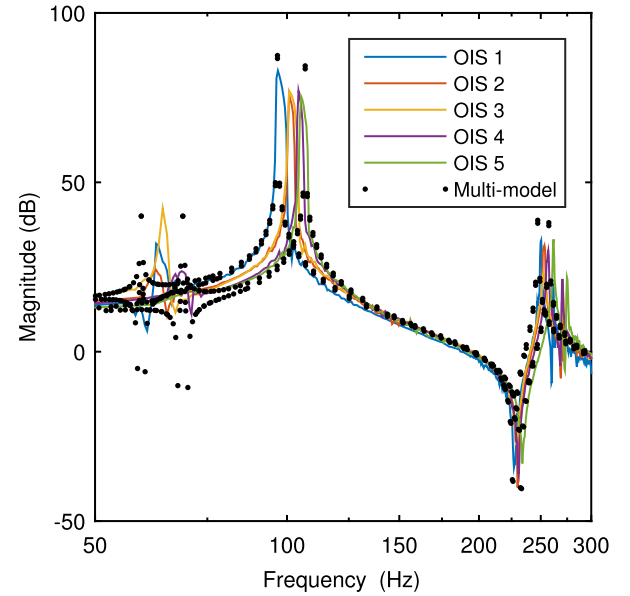


Fig. 11. Frequency response data measured from individual experimental prototypes by experimental setup and proposed multi model capturing product variabilities.

Table 5

Experimental closed-loop stability analysis results of nominal conventional controllers and designed robust controllers implemented on five large scale prototypes.

	OIS 1	OIS 2	OIS 3	OIS 4	OIS 5
PID	×	×	✓	✓	✓
lead–lag	×	×	✓	✓	✓
LQR	✓	✓	✓	×	×
H_∞	×	×	✓	✓	✓
μ -synthesis	✓	✓	✓	✓	✓
Robust H_∞	✓	✓	✓	✓	✓

& Safonov, 2008) based on the μ -synthesis control theory (Packard & Doyle, 1993). The μ -synthesis controller design technique is iterative. The controller is designed with 10 iterations leading to performance upper-bound of 0.87 on structured singular value.

The closed-loop stability of the designed controllers is analyzed experimentally to account for modeling errors. Table 5 shows the experimental results of closed-loop stability. In this experiment, the designed controllers in each row are implemented on different prototypes in each column. If the closed-loop system corresponding to the controller and the prototype was stable, the cell at the intersection of the row associated with the controller and the column associated with the prototype is designated by the check mark (✓); otherwise it is designated by the cross mark (×). According to Table 5, none of nominal controllers can stabilize the closed-loop system corresponding to all OISs because the nominal controller design methods do not take uncertainties into account. On the other hand, both robust controllers (robust H_∞ controller and μ -synthesis controller) stabilized the closed-loop system for all prototypes (S1) because the robust controller design methods guarantee robust closed-loop stability against uncertainties in the design stage.

Fig. 12 shows RMS values of the tracking errors of different controllers. Real hand-shake data are collected and used for time-domain performance assessment. Details about hand-shake data are presented in Appendix E. In Fig. 12, the cross mark (×) and error bars, respectively, indicate the mean value and standard deviations of the RMS errors for different hand-shakes data profiles and OIS prototypes. For the nominal controllers, their de-tuned versions are used for the closed-loop experiments to recover robust stability for all plants (OIS 1–5).

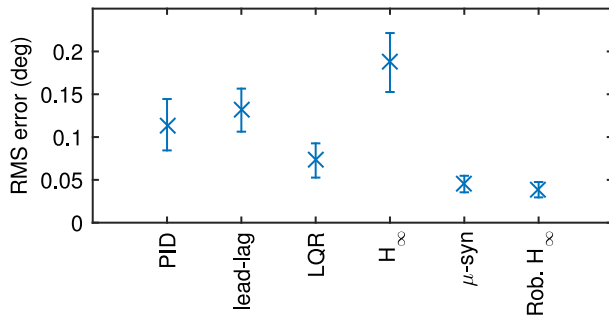


Fig. 12. RMS error of controllers on various prototypes subject to different hand-shakes.

Table 6

Comparisons of robust H_∞ with μ -synthesis on five large scale prototypes with nominal and worst-case performances presented outside and inside parentheses, respectively.

	μ -synthesis	Robust H_∞
Designed order (–)	76	11
Reduced order (–)	18	9
Tracking error (deg)	0.0451 (0.0082)	0.0385 (0.0079)
Control effort (mAh)	0.4556 (0.1153)	0.4555 (0.1152)
Computation time (s)	75	269

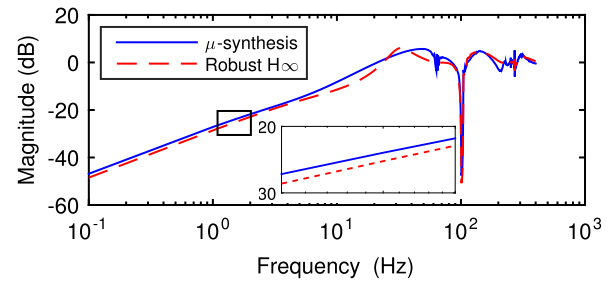
De-tuning refers to a heuristic approach of making a designed controller less aggressive to increase robustness. To de-tune, a design parameter that best represents trade-off of closed-loop performance and robustness in each controller design method (such as proportional gain in classical controller design methods) is adjusted in the corresponding controller designed for OIS 3 to increase robustness such that the controller stabilizes the closed-loop system for the uncertainty region.

As shown in Fig. 12, the conventional nominal controller design approach with heuristic de-tuning brings about significant performance degradation. On the other hand, μ -synthesis controller and robust H_∞ controller can provide almost as good performance as nominal controllers while stabilizing all prototypes because they consider uncertainties explicitly in the model and controller design, and utilize optimization tools to prevent conservative design.

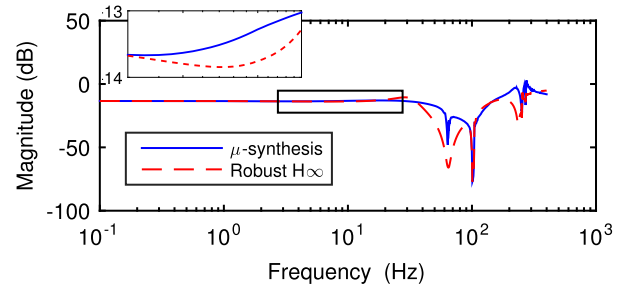
The robust H_∞ controller is compared with only μ -synthesis controller more extensively because only these two controllers in this paper are robust controllers equipped with systematic optimization against uncertainties. Due to lack of systematic optimization, the performance of the conventional nominal controllers degraded significantly as shown in Fig. 12. Therefore, they are not considered as potential candidates for more extensive comparisons.

The robust H_∞ controller is compared with the μ -synthesis controller in terms of controller order, tracking error, control effort, and computation time in Table 6. The controller order for the robust H_∞ controller was much smaller than that of the μ -synthesis controller (O4) because the robust H_∞ controller design method theoretically constrains the controller order. The controller order reduction was performed by standard model reduction techniques. The controller order was reduced as long as closed-loop stability and closed-loop performance specifications are not violated for the entire uncertainty region (5) and (6). Then, the tracking error and control effort measurements were performed based on the reduced order controller. For tracking error and control effort, the values outside parentheses are mean values, while the ones between parentheses are the worst-case degradations. The robust H_∞ controller slightly reduced mean (O1) and degradation (O3) of the tracking error as well as the mean (O2) and the degradation (O3) of the control effort compared to the μ -synthesis controller. The reduction in tracking error was about 15%.

The experimental result in time-domain were consistent with closed-loop frequency response in Fig. 13, which shows a comparison of the



(a) Transfer function from reference to tracking error



(b) Transfer function from reference to control input

Fig. 13. Comparisons between μ -synthesis and robust H_∞ controllers in frequency-domain on the nominal prototype (OIS 3).

nominal sensitivity functions for robust H_∞ controller and μ -synthesis controller. In general, the sensitivity transfer functions have similar shapes; however, the robust H_∞ controller has slightly less error and control input in the low-frequency region, as shown in the enlarged part in the figure. The black rectangle in the figure shows the region that is enlarged for better comprehension.

In Fig. 14, experimental results in time-domain are plotted where robust controllers are implemented on the nominal prototype OIS 3 subjected to one of hand-shake data. The black solid line indicates the original hand-shake disturbance affecting the camera. The red dashed line and the blue dashed-dotted lines show the tracking error signal after implementation of the μ -synthesis and robust H_∞ controller, respectively. It can be seen that the robust H_∞ controller rendered slightly smaller tracking errors and control input than μ -synthesis controller. The superiority of the robust H_∞ is due to the lower sensitivity and the lower input sensitivity over low-frequencies in Fig. 13.

6. Conclusion

Robust control of the magnetically-actuated lens-tilting optical image stabilizer was presented in this paper. A finite element analysis was performed to capture the structure of dynamics and uncertainties due to beam width variations of lens-platform and force imbalance of the moving-magnet actuators. A dynamic uncertainty model was developed based on the finite element analysis results. A robust H_∞ controller was designed for the uncertainty model. The experimental results demonstrates that the designed robust H_∞ achieves robust stability with better robust tracking performance than the conventional nominal controllers. Moreover, experimental results implied feasibility of the proposed method in an experimental setting and its capability to deal with physical product variabilities. Finally, the robust H_∞ controller was shown to outperform μ -synthesis controller by 15% in tracking and to achieve much lower controller order for practical implementation on mobile phone devices.

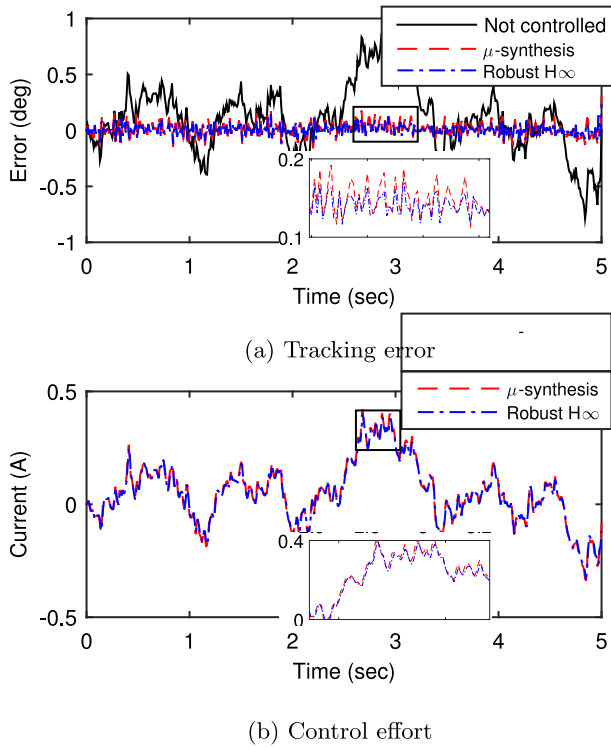


Fig. 14. Comparisons between μ -synthesis and robust H_∞ controllers in time-domain demonstrated on nominal prototype (OIS 3).

Acknowledgments

This work was supported by the Natural Sciences and Engineering Research Council of Canada (NSERC) Strategic Project Grant and the Institute for Computing, Information and Cognitive Systems (ICICS), Canada at University of British Columbia.

Appendix A. Moving-magnet actuator modeling

The moving-magnet actuators from current inputs to torque output display static nonlinear behavior. Therefore, we will model the moving-magnet actuator as a static map, i.e., the 'Look-up Table' block in Fig. 2, and obtain its inverse map to compensate for its nonlinearity.

The model of the moving-magnet actuators is developed considering the currents of coils as the input and the torque generated on the lens-platform about the x -axis as the output. Fig. 15 illustrates the tilt actuation about one axis. A torque T is generated on the lens-platform by forces F generated on the magnets by coils with the configuration shown.

The forces F necessary to generate a torque T can be obtained as

$$F = T/4r. \quad (21)$$

The force generated on the magnet is a function of the current of the coil and the air-gap. According to Lorentz's law, force is linearly proportional to the current, and due to Ampere's law, it was inversely related to the air-gap. To quantitatively obtain this relationship, finite-element method magnetics (FEMM) software (Meeker, 2015) is used for the parameters of moving-magnet actuators in Table 2. Fig. 16 shows the inverse relationship of the force with the air-gap for a constant current of 1 A as obtained by FEMM.

This relationship is used as a look-up table denoted by $p(z)$ where z is the air-gap. Hence, the force generated on each magnet can be described as $F = p(z)I$, where I is the current supplied to the coil. When the lens-platform tilts θ about x -axis, air-gaps of pairs of coil/magnet

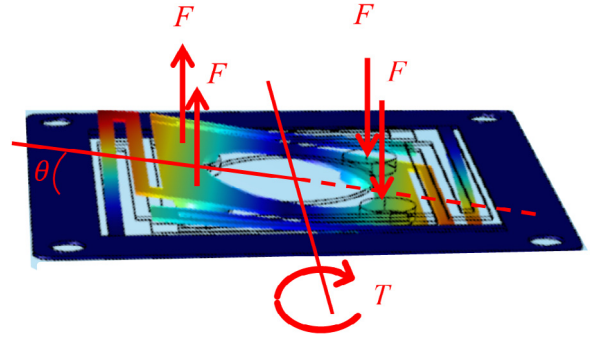


Fig. 15. Configuration of magnetic forces when actuating one of tilting DOFs used in modeling actuators and FEA.

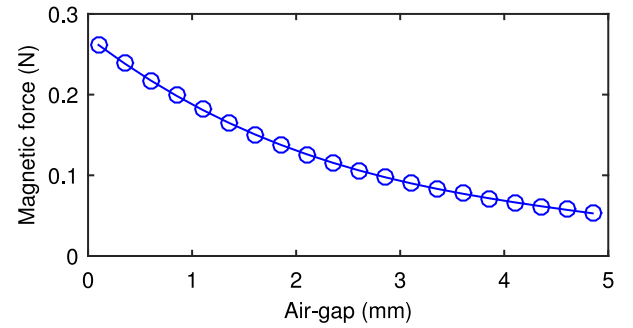


Fig. 16. Force–air-gap relationship for a constant current of 1 A obtained by FEA and used in look up table.

on two sides of this axis can be calculated as $z_{1,3} = z_0 - r \sin(\theta)$ and $z_{2,4} = z_0 + r \sin(\theta)$, where z_0 is the equilibrium air-gap, r is the distance of magnets from central axes, and the z_k ($k = 1, 2, 3, 4$) is the air-gap of the k th moving-magnet actuator. These air-gap values of each actuator is used to calculate the required current to be applied to its coil (i_k) by $i_k = F/p(z_k)$.

Appendix B. Derivation of the closed-loop state-space matrices

This section explains the derivation of the state-space parameters of the closed-loop system $\mathcal{T}_{rz,i}$ from the state-space parameters of the augmented plant (11) and the controller (14). The index i is dropped for simplicity of comprehension. Based on (11), the state-space equations of the generalized plant can be written as:

$$\dot{x} = Ax + B_r r + B_u u \quad (22)$$

$$z = C_z x + D_{zr} r + D_{zu} u \quad (23)$$

$$e = C_e x + D_{er} r \quad (24)$$

where, x is the state variable of the generalized plant. Similarly, (14) and Figure 8 suggest that the state-space equations of the controller can be written as:

$$\dot{x}_K = A_K x_K + B_K e \quad (25)$$

$$u = C_K x_K + D_K e \quad (26)$$

where, x_K is the state variable of the controller. By substituting e in (26), u can be written independent of e as:

$$u = D_K C_e x + C_K x_K + D_K D_{er} r \quad (27)$$

Using (24) and (27), e and u can be eliminated from the rest of the state-space equations (i.e., (22), (25), and (23)) leading to the state-space equations of the closed-loop system as follows:

$$\dot{x} = (A + B_u D_K C_e)x + B_u C_K x_K + (B_r + B_u D_K D_{er})r \quad (28)$$

$$\dot{x}_K = B_K C_e x + A_K x_K + B_K D_{er} r \quad (29)$$

$$z = (C_z + D_{zu} D_K C_e)x + D_{zu} C_K x_K + (D_{zr} + D_{zu} D_K D_{er})r \quad (30)$$

Based on (28)–(30), the state-space matrices of the closed-loop system $\mathcal{T}_{r,z,i}$ can be denoted as:

$$\left[\begin{array}{cc|c} A + B_u D_K C_e & B_u C_K & B_r + B_u D_K D_{er} \\ B_K C_e & A_K & B_K D_{er} \\ \hline C_z + D_{zu} D_K C_e & D_{zu} C_K & D_{zr} + D_{zu} D_K D_{er} \end{array} \right]. \quad (31)$$

The state-space parameters of the closed-loop system depends linearly on the state-space parameters of the controller. Using notations (16)–(17), (31) can be reorganized as (15) such that its elements depend on a single controller parameter matrix Θ which is more efficient for linear optimization.

Appendix C. Reformulation of multi-model robust H_∞ controller design problem to matrix inequalities using bounded real lemma

This section explains reformulation of the multi-model robust H_∞ controller design problem (13) to the matrix inequalities in (18). As the H_∞ norm is a positive value, the multi-model robust H_∞ controller design problem (13) can be written as:

$$\text{minimize } \gamma, \text{ subject to } \max_i \|\mathcal{T}_{r,z,i}(\Theta)\|_\infty < \gamma \quad (32)$$

where γ is a positive real variable. Eq. (32) can be written as the following equation because the norms of all closed-loop systems associated with multi-model has to be less than γ in order for the norm of the worst-case closed-loop system to be less than γ .

$$\text{minimize } \gamma, \text{ subject to } \|\mathcal{T}_{r,z,i}(\Theta)\|_\infty < \gamma, \forall i \quad (33)$$

According to the bounded real lemma, for a system $T(s) = C(sI - A)^{-1}B + D$, we have $\|T(s)\|_\infty < \gamma$ if and only if there exists $P > 0$ that solves the LMI:

$$\begin{bmatrix} \langle PA \rangle & PB & C^T \\ * & -\gamma I & D^T \\ * & * & -\gamma I \end{bmatrix} < 0, \quad (34)$$

In (33), $T(s)$ corresponds to $\mathcal{T}_{r,z,i}(s)$ with the state-space realization (15). By substituting this state-space realization, the matrix in (34) transforms to the following matrix:

$$\begin{bmatrix} \langle P_i A_{0,i} + P_i B_i \Theta C_i \rangle & P_i B_{0,i} + P_i B_i \Theta D_{yr,i} & C_{0,i}^T + C_i^T \Theta^T D_{zu,i}^T \\ * & -\gamma I & D_{zr,i}^T + D_{yr,i}^T \Theta^T D_{zu,i}^T \\ * & * & -\gamma I \end{bmatrix}, \quad (35)$$

The terms without Θ can be denoted as $\Psi_i(P_i, \gamma)$ and extracted as (19) leading to the following matrix summation:

$$\Psi_i(P_i, \gamma) + \begin{bmatrix} \langle P_i B_i \Theta C_i \rangle & P_i B_i \Theta D_{yr,i} & C_i^T \Theta^T D_{zu,i}^T \\ * & 0 & D_{zr,i}^T \Theta^T D_{zu,i}^T \\ * & * & 0 \end{bmatrix}, \quad (36)$$

As shown above, the remaining matrix is of a quadratic form with Θ or Θ^T participating in all elements. Therefore, this matrix can be written as:

$$\Psi_i(P_i, \gamma) + Q_i^T \Theta^T P_i + P_i^T \Theta Q_i, \quad (37)$$

where

$$P_i^T \Theta Q_i = \begin{bmatrix} P_i B_i \Theta C_i & P_i B_i \Theta D_{yr,i} & 0 \\ 0 & 0 & 0 \\ D_{zu,i} \Theta C_i & D_{zu,i} \Theta D_{yr,i} & 0 \end{bmatrix}, \quad (38)$$

By inspection, P_i and Q_i can be determined from the above equation as presented in (20).

Appendix D. Initially-feasible controller design

In this section, we present a modified version of the procedure proposed in Kanev et al. (2004) to design an initially-feasible controller as the initial guess to solve the non-convex optimization problem (18). The procedure is modified to deal with multi-model, rather than polytopic uncertainty model which was the focus of Kanev et al. (2004). The procedure involves two steps corresponding to design of state-feedback and initially-feasible output-feedback controller as follows.

D.1. State-feedback controller design

The goal is to design a state-feedback gain C_K for multi-model (11) such that it stabilizes the closed-loop system and optimizes the robust H_∞ performance

$$\max_i \|\mathcal{T}_{r,z,i}(C_K)\|_\infty. \quad (39)$$

Theorem 6 in Kanev et al. (2004) states that this problem can be formulated as a convex optimization problem based on LMIs:

$$\min_{L, Q} \gamma, \text{ s.t. } \begin{bmatrix} -\langle \mathbb{A}_i \rangle & B_{r,i} & \mathbb{C}_i^T \\ * & I & D_{zr,i}^T \\ * & * & \gamma I \end{bmatrix} > 0, \forall i, \quad (40)$$

where $\mathbb{A}_i := A_i Q + B_{u,i} L$, $\mathbb{C}_i := C_{z,i} Q + D_{zu,i} L$, and $Q > 0$. Using the solutions L and Q , the optimal state-feedback controller is given as $C_K := LQ^{-1}$.

D.2. Output-feedback controller design

To design an initially-feasible output-feedback controller, the designed state-feedback controller is set for C_K and $D_K = 0$ in (14). By doing this, problem (15) is formulated as a convex problem based on LMIs (Theorem 8 in Kanev et al. (2004):

$$\min_{\substack{X_i > 0, Y > 0 \\ Z, G}} \gamma, \text{ s.t. } \begin{bmatrix} -\langle M_i \rangle & N_i & \Omega_i^T \\ * & I & D_{zr,i}^T \\ * & * & \gamma I \end{bmatrix} > 0, \forall i. \quad (41)$$

Here, the matrices M_i , N_i , and Ω_i are defined as

$$M_i := \begin{bmatrix} X_i(A_i + B_{u,i} C_K) & -X_i B_{u,i} C_K \\ M_{21,i} & Z + G D_{yu,i} F - Y B_{u,i} C_K \end{bmatrix},$$

$$N_i := \begin{bmatrix} X_i B_{r,i} \\ Y B_{r,i} - G D_{yr,i} \end{bmatrix},$$

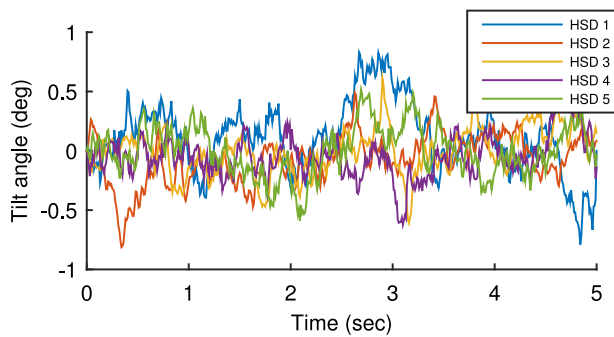
$$\Omega_i := [C_{z,i} + D_{zu,i} C_K \quad -D_{zu,i} C_K].$$

Using the solutions Z , G , and Y , controller parameters can be obtained as $A_K := Y^{-1} Z$ and $B_K := Y^{-1} G$.

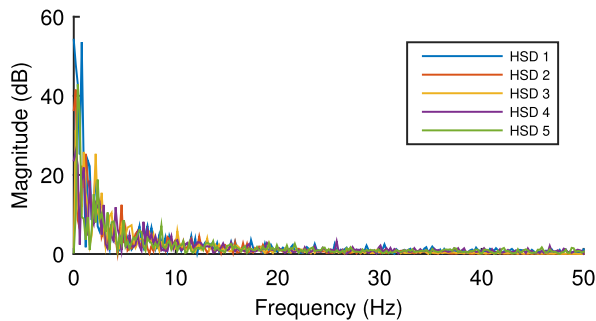
Appendix E. Hand-shake disturbance database

To evaluate designed controllers in the time-domain, real hand-shake disturbance data are collected from built-in gyro-enhanced motion sensors of a mobile phone while holding the mobile phone to take a photograph. A data set is prepared by hand-shake disturbance data of 5 different people as displayed Fig. 17(a), where HSD stands for hand-shake data.

To validate the data set, a spectral analysis is performed on this data set. Fig. 17(b) shows the spectral density for each of 5 hand-shake data in the data set. As shown, the spectral density of different hand-shake data are consistent with each other as well as the results published in the literature (Golik, Fischer, & Wueller, 2006; Song et al., 2009).



(a) Time-domain signals



(b) Frequency-domain spectra

Fig. 17. Real hand-shake disturbance data measured by gyro sensor of a mobile phone for 5 different people holding it while taking picture.

References

- Alizadegan, A., Zhao, P., Nagamune, R., & Chiao, M. (2016). Modeling and robust control of miniaturized magnetically-actuated optical image stabilizer. In *Proceedings of the IEEE international conference on advanced intelligent mechatronics* (pp. 846–851).
- Balas, G., Chiang, R., Packard, A., & Safonov, M. (2008). Robust control toolbox, For Use with Matlab. User's Guide, Version 3.
- Chang, H. J., Kim, P. J., Song, D. S., & Choi, J. Y. (2009). Optical image stabilizing system using multirate fuzzy PID controller for mobile device camera. *IEEE Transactions on Consumer Electronics*, 55(2), 303–311.
- Chiu, C.-W., Chao, P. C.-P., Kao, N. Y.-Y., & Young, F.-K. (2008). Optimal design and experimental verification of a magnetically actuated optical image stabilization system for cameras in mobile phones. *Journal of Applied Physics*, 103(7) 07F136–1–07F136–3.
- Fei, J., & Batur, C. (2007). A novel adaptive sliding mode controller for MEMS gyroscope. In *Proceedings of the 46th IEEE conference on decision and control* (pp. 3573–3578).
- Fei, J., & Zhou, J. (2012). Robust adaptive control of MEMS triaxial gyroscope using fuzzy compensator. *IEEE Transactions on Systems, Man, and Cybernetics, Part B: Cybernetics*, 42(6), 1599–1607.
- Golik, B., Fischer, G., & Wueller, D. I. D. (2006). *Development of a test method for image stabilizing systems*. Cologne University of Applied Sciences.
- Hao, Q., Cheng, X., Kang, J., & Jiang, Y. (2015). An image stabilization optical system using deformable freeform mirrors. *Sensors*, 15(1), 1736–1749.
- Harno, H. G., & Woon, R. S. K. (2015). Robust H_∞ stabilization of a hard disk drive system with a single-stage actuator. In *Proceedings of the IOP conference series: Materials science and engineering* (pp. 969–975).
- Heckele, M., & Schomburg, W. (2004). Review on micro molding of thermoplastic polymers. *Journal of Micromechanics and Microengineering*, 14(3), R1–R14.
- Herrmann, G., & Guo, G. (2004). HDD dual-stage servo-controller design using a μ -analysis tool. *Control Engineering Practice*, 12(3), 241–251.
- Huang, X., Horowitz, R., & Li, Y. (2005). Design and analysis of robust track-following controllers for dual-stage servo systems with an instrumented suspension. In *Proceedings of the American control conference* (pp. 1126–1131).
- Huang, X., Nagamune, R., & Horowitz, R. (2006). A comparison of multirate robust track-following control synthesis techniques for dual-stage and multisensing servo systems in hard disk drives. *IEEE Transactions on Magnetics*, 42(7), 1896–1904.
- Izadbakhsh, A., & Rafiei, S. (2008). Robust control methodologies for optical micro electro mechanical system-new approaches and comparison. In *Proceedings of the power electronics and motion control conference* (pp. 2102–2107).
- Kanev, S., Scherer, C., Verhaegen, M., & de Schutter, B. (2004). Robust output-feedback controller design via local BMI optimization. *Automatica*, 40(7), 1115–1127.
- Komori, M., & Hirakawa, T. (2005). A magnetically driven linear microactuator with new driving method. *IEEE/ASME Transactions on Mechatronics*, 10(3), 335–338.
- Kwon, S. (2004). *Micromachined lens scanning confocal microscope array for micro total analysis systems* (Ph.D. thesis), University of California at Berkeley.
- Lee, C., & Salapaka, S. M. (2009). Fast robust nanopositioning: A linear-matrix-inequalities-based optimal control approach. *IEEE/ASME Transactions on Mechatronics*, 14(4), 414–422.
- Lee, S.-K., & Kong, J.-H. (2014). An implementation of closed-loop optical image stabilization system for mobile camera. In *Proceedings of the IEEE international conference on consumer electronics* (pp. 45–46).
- Lee, S.-K., Kook, I.-H., & Kong, J.-H. (2012). A study of mobile optical image stabilization system for mobile camera. In *Proceedings of the international SoC design conference* (pp. 212–214).
- Li, T.-H. S., & Chen, C.-C. (2013). Extended Kalman filter based hand-shake detector for optical image stabilization using a low cost gyroscope. *IEEE Transactions on Consumer Electronics*, 59(1), 113–121.
- Li, T.-H. S., Chen, C.-C., & Su, Y.-T. (2012). Optical image stabilizing system using fuzzy sliding-mode controller for digital cameras. *IEEE Transactions on Consumer Electronics*, 58(2), 237–245.
- Li, W., & Liu, P. X. (2009). Robust adaptive tracking control of uncertain electrostatic micro-actuators with H_∞ performance. *Mechatronics*, 19(5), 591–597.
- Li, W., & Liu, P. X. (2011). Adaptive tracking control of an MEMS gyroscope with H_∞ performance. *Journal of Control Theory and Applications*, 9(2), 237–243.
- Li, Y., & Horowitz, R. (2001). Mechatronics of electrostatic microactuators for computer disk drive dual-stage servo systems. *IEEE/ASME Transactions on Mechatronics*, 6(2), 111–121.
- Lin, C.-Y., & Chiou, J.-C. (2011). Design, fabrication and actuation of four-axis thermal actuating image stabiliser. *IET Micro & Nano Letters*, 6(7), 549–552.
- Malisoff, M., Mazenc, F., & de Queiroz, M. (2008). Tracking and robustness analysis for controlled microelectromechanical relays. *International Journal of Robust and Nonlinear Control*, 18(18), 1637–1656.
- Meeker, D. (2015). Finite element method magnetics Version 4.2 (25Oct2015 Build), <http://www.femm.info>.
- Nagamune, R., Huang, X., & Horowitz, R. (2010). Robust control synthesis techniques for multirate and multisensing track-following servo systems in hard disk drives. *Journal of Dynamic Systems, Measurement, and Control*, 132(2) 021005–1–021005–10.
- Packard, A., & Doyle, J. (1993). The complex structured singular value. *Automatica*, 29(1), 71–109.
- Palm, R. (1994). Robust control by fuzzy sliding mode. *Automatica*, 30(9), 1429–1437.
- Pournazari, P., Nagamune, R., & Chiao, M. (2014). A concept of a magnetically-actuated optical image stabilizer for mobile applications. *IEEE Transactions on Consumer Electronics*, 60(1), 10–17.
- Sarraf, E. H., Sharma, M., & Cretu, E. (2011). Novel sliding mode control for MEMS-based resonators. *Procedia Engineering*, 25, 1305–1308.
- Sarraf, E. H., Sharma, M., & Cretu, E. (2012). Novel band-pass sliding mode control for driving MEMS-based resonators. *Sensors Actuators A*, 186, 154–162.
- Shavezpur, M., Ponnambalam, K., Khajepour, A., & Hashemi, S. (2008). Fabrication uncertainties and yield optimization in MEMS tunable capacitors. *Sensors Actuators A*, 147(2), 613–622.
- Song, M.-G., Baek, H.-W., Park, N.-C., Park, K.-S., Yoon, T., Park, Y.-P., et al. (2010). Development of small sized actuator with compliant mechanism for optical image stabilization. *IEEE Transactions on Magnetics*, 46(6), 2369–2372.
- Song, M.-G., Hur, Y.-J., Park, N.-C., Park, Y.-P., Park, K.-S., & Lim, S.-C., et al. (2009). Development of small sized actuator for optical image stabilization. In *Proceedings of the international symposium on optomechatronic technologies* (pp. 152–157).
- Song, X., Gillella, P. K., & Sun, Z. (2015). Low-order stabilizer design for discrete linear time-varying internal model-based system. *IEEE/ASME Transactions on Mechatronics*, 20(6), 2666–2677.
- Sun, Y., Fowkes, C. R., Gindy, N., & Leach, R. K. (2010). Variation risk analysis: MEMS fabrication tolerance for a micro CMM probe. *The International Journal of Advanced Manufacturing Technology*, 47(9–12), 1113–1120.
- Tzafestas, S. G., & Rigatos, G. G. (1999). A simple robust sliding-mode fuzzy-logic controller of the diagonal type. *Journal of Intelligent and Robotic Systems*, 26(3–4), 353–388.
- Yan, G. Y., Liu, Y. B., & Feng, Z. H. (2015). A dual-stage piezoelectric stack for high-speed and long-range actuation. *IEEE/ASME Transactions on Mechatronics*, 20(5), 2637–2641.
- Yeom, D. (2009). Optical image stabilizer for digital photographing apparatus. *IEEE Transactions on Consumer Electronics*, 55(5), 1028–1031.
- Yeom, D., Park, N., & Jung, S. (2007). Digital controller of novel voice coil motor actuator for optical image stabilizer. In *Proceedings of the international conference on control, automation and systems* (pp. 2201–2206).
- Yu, H.-C., & Liu, T. (2008a). Adaptive model-following control for slim voice coil motor type optical image stabilization actuator. *Journal of Applied Physics*, 103(7) 07F114–1–07F114–3.
- Yu, H.-C., & Liu, T. (2008b). Sliding mode control using virtual eigenvalue method for compact optical image stabilization actuators. *IEEE Transactions on Magnetics*, 44(11), 4074–4077.

- Yuan, K. (2015). *A 3D printing and moulding method of the fabrication of a miniature voice coil motor actuator* (Master's thesis), University of British Columbia.
- Zhang, X., Koo, B., Salapaka, S. M., Dong, J., & Ferreira, P. M. (2014). Robust control of a mems probing device. *IEEE/ASME Transactions on Mechatronics*, 19(1), 100–108.
- Zhao, P., Alizadegan, A., Nagamune, R., & Chiao, M. (2015). Robust control of large-scale prototypes for miniaturized optical image stabilizers with product variations. In *Proceedings of the 54th annual conference of the society of instrument and control engineers of Japan (SICE)* (pp. 734–739).
- Zhou, K., Doyle, J. C., & Glover, K. (1996). *Robust and optimal control*. New Jersey: Prentice Hall.
- Zhu, G., Penet, J., & Saydy, L. (2006). Robust control of an electrostatically actuated MEMS in the presence of parasitics and parametric uncertainties. In *Proceedings of the American control conference* (pp. 1233–1238).